JMEPEG (2009) 18:339–350
DOI: 10.1007/s11665-008-9298-1

1059-9495/$19.00

Numerical and Experimental Investigations on the Loads Carried by the Tool During Friction Stir Welding

Hosein Atharifar, Dechao Lin, and Radovan Kovacevic

(Submitted November 26, 2007; in revised form July 15, 2008)

A computational fluid dynamics (CFD) model is presented for simulating the material flow and heat transfer in the friction stir welding (FSW) of 6061-T6 aluminum alloy (AA6061). The goal is to utilize the 3-D, numerical model to analyze the viscous and inertia loads applied to the FSW tool by varying the welding parameters. To extend the FSW process modeling, in this study, the temperature-dependant material properties as well as the stick/slip condition are considered where the material at the proximity of the FSW tool slips on the lower pressure regions. A right-handed one-way thread on a tilted FSW tool pin with a smooth, concaved shoulder is, additionally, considered to increase the accuracy of the numerical model. In addition, the viscous and frictional heating are assumed as the only sources of heat input. In the course of model verification, good agreements are found between the numerical results and the experimental investigations.

Keywords CFD, experiments, friction stir welding (FSW), loads, numerical analysis

1. Introduction

As a solid-state joining technique, friction stir welding (FSW) (Ref 1) has been a prominent process in welding similar and dissimilar aluminum alloys (Ref 2). This process is being used in wide variety of applications in the automotive, aerospace, ship building, and railroad industries (Ref 3). To facilitate and enhance the evolution of the FSW process, numerical analysis may be utilized in designing the optimized tool geometry, estimating and minimizing the required process power, and increasing the welding speed without diminishing strength of the joint.

To understand the weld characteristics and material flow behavior in the FSW process, substantial work has been performed and published in literature. The research areas that have been focused on primarily are the microstructure and material properties of the joint (Ref 4, 5), welding of high strength materials (Ref 6), advancement in FSW tool design (Ref 7), thermal and structural modeling (Ref 8, 9), material flow visualization (Ref 10-14), and material flow modeling (Ref 15-17). The material flow visualization is mainly performed experimentally where non-coherent types of materials in the form of tracers such as powder, shots, inserts, and specimens of dissimilar material are used to visualize the material flow inside the nugget and thermo-mechanical affected zone (TMAZ). Numerical simulations of material flow are also performed in order to fundamentally understand thermo-physical and thermo-mechanical variations in the material properties (Ref 16), and to study the effect of process parameters on the peak temperature and pressure distribution (Ref 15, 16). In the FSW process, the urgent need to recognize the amount of required clamping forces, in addition to avoiding tool pin failure, and evaluating the expenditure of energy for a typical welding process oblige having a fundamental understanding of the extent of the loads applied to the tool under different welding parameters. The initiation of any load and its variations arise from material flow characteristics and the variation of material properties in the plasticized region. Basically, any stationary body subjected to the flow of material is affected in terms of the loads at the body-fluid interface. Longitudinal (drag), axial (lift), and lateral (side) forces as well as the moment (torque) are the integral or resultant loads applied to the body through the flow of material. These loads are complex to compute analytically or numerically due to their relations with the distribution of pressure and shear stress in the body-flow interface.

Colegrove and Shercliff (Ref 15) used computational fluid dynamics (CFD) to numerically analyze the material flow and heat transfer of the FSW process. They assumed a threaded FSW tool pin with a normal axis as well as one with a rake-angle of 2.25 degrees. They compared the numerically computed and experimentally measured traverse forces applied to the FSW tool. Their numerical results overestimated the amount of heat input, and they had poor predictions of the welding forces. Nevertheless, they showed that the numerically computed traverse force is 50% less for the tilted tool than for the tool with a normal axis. The shortcoming in the Colegrove and Shercliff model may be overcome with assuming the material slip at the tool interface. Likewise, Crawford et al. (Ref 18) implemented an experimental and numerical analysis to estimate the loads and required power for the FSW process. Their investigation was to resolve the requirements for a firm backplate (support) in a typical FSW process. Therefore, their experiments and

Hosein Atharifar, Department of Industry and Technology, Millersville University, Millersville, PA 17551; and **Dechao Lin** and **Radovan Kovacevic**, Research Center for Advanced Manufacturing, Southern Methodist University, Dallas, TX 75205. Contact e-mail: hatharifar@millersville.edu.

numerical models were setup in high rotational velocity range (1500-4500 rpm). They used *Viscoplastic* and *Couette* material models in FLUENT (Lebanon, NH) and compared the numerical results with their experiments. Their numerical results converged approximately to the experimental outcomes when the rotational velocity exceeded 2500 rpm. In addition, Chen et al. (Ref 19) developed a finite element code using ANSYS parametric design language (APDL) (Canonsburg, PA) to estimate the loads applied to the tool for 6061-T6 aluminum alloy (AA6061) and AISI 1018 steel. Their proposed local model enabled the simulation of longitudinal and axial forces variation over time. Furthermore, they changed the traverse and rotational velocity of the tool and plotted the variation of nodal maximum forces. Regardless of their simplified model with a smooth pin and solely a frictional heat input, they presented a good agreement between the numerical model and experimental investigations. Further studies on the loads carried by the tool were accomplished by (Ref 20-23). Apart from the total number of investigations, the extent of the loads carried by the tool in the FSW process and the power required to operate the process have been little discussed. For example, the extent of the viscous and inertia loads, the effect of temperature-dependant material properties, and the true model of the FSW tool must be considered in order to obtain an accurate prediction of the loads.

In this study, a numerical analysis of the material flow and heat transfer is performed for the FSW of AA6061-T6. The FSW tool is modeled with a rake-angle of 2.5 degrees, equipped with a concaved, smooth shoulder, and a cylindrical pin with a one-way, right-handed thread. FLUENT is employed to solve the coupled thermal and fluid flow equations. The heat input sources are assumed as (1) frictional and shear heating when the sliding/sticking condition of the FSW tool with the surrounding material is assumed, and (2) viscous heating of the material deformation. The constitutive law for the plasticized material is selected based on the viscoplastic material model, and appropriate coefficients are selected according to the coefficients used in the hot extrusion of the AA6061. The thermal model is verified by the measured temperature at different locations underneath the specimen. The material flow model is verified by conducting axial force measurements for different welding parameters. The results are presented in the form of material flow characteristics as well as the physical properties of the plasticized region. In addition, longitudinal, axial, and lateral forces along with moment about the tool axis are numerically computed, and the mean values of the loads are presented for different welding parameters. Finally, the extent of the loads and the required power of the process under various welding parameters are pinpointed and discussed.

2. Physical Concepts

FSW as a combined forming and joining process is susceptible to various process conditions. The quality of friction stir (FS) welds is vulnerable depending on the flatness of the machine bed, the accuracy of the machine axis, the clamping forces, the tool material, the morphology of the tool pin and shoulder, the backing plate and specimen material properties, and other independent process variables. An engineering approach for observing the effect of the welding parameters on the loads carried by the FSW tool may be initiated by preparing a physical schematic of the process prior to modeling it numerically.

The material flow in the FSW process is similar to a benchmark fluid mechanics problem (Ref 24, 25) in which a rotating cylinder is subjected to a uniform motion of the material flow. Identically, in the FSW process, the circulation of the tool pin and shoulder inside the plasticized material develops an asymmetric flow field around the tool with deviatoric velocity and pressure fields. Besides, the momentum transport from the shoulder adds to the complexity of the material flow analysis, and in order to obtain an accurate simulation of the material flow, the process should be modeled in 3-D. In the FSW process, instead of modeling the traverse motion of the tool, it is more computationally inexpensive to assume that the surrounding plasticized material moves with a uniform free-stream velocity equal to the traverse velocity (v) of the tool, while the rotating tool stays stationary. Figure 1 illustrates an analogous schematic view of the flow past a rotary cylinder for the FSW setup. In this figure, the uniform and non-uniform streamlines passing the pin are observed due to a non-rotating (see Fig. 1a) and rotating (see Fig. 1b) tools, respectively. The lateral force (S) shown in Fig. 1(b), is created due to the *Magnus effect* exists in the material flow around the rotary pin. Furthermore, due to the upstream and downstream pressure deviations in the boundary layer around the FSW tool, a longitudinal force (D) is acting on the tool along x-axis with different magnitudes for the non-rotating (see Fig. 1a) and rotating (see Fig. 1b) tool.

Former studies affirm that the viscous, non-Newtonian fluid resembles a solid material flow during forging and extrusion (Ref 26). FSW can be categorized as a high speed non-homogeneous forming process that encompasses the material extrusion and forging (Ref 27). Due to this similarity, the flow region in the FSW process may be treated as a *rate-dependant* plasticized material or so-called *viscoplastic* material (Ref 28).

Figure 2 illustrates the schematic front-view of the FSW tool inclined at 2.5 degrees with respect to the traveling direction. As it is depicted, the material enters into the computational zone with the free-stream velocity equal to the traverse velocity of the FSW tool (v). At the same time, the FSW tool is rotated around its axis with a angular velocity

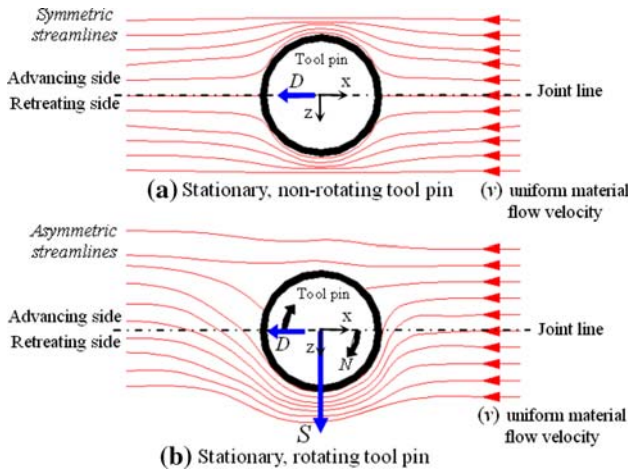

Fig. 1 Uniform flow of the material passes the (a) non-rotating and (b) rotating FSW tool pin

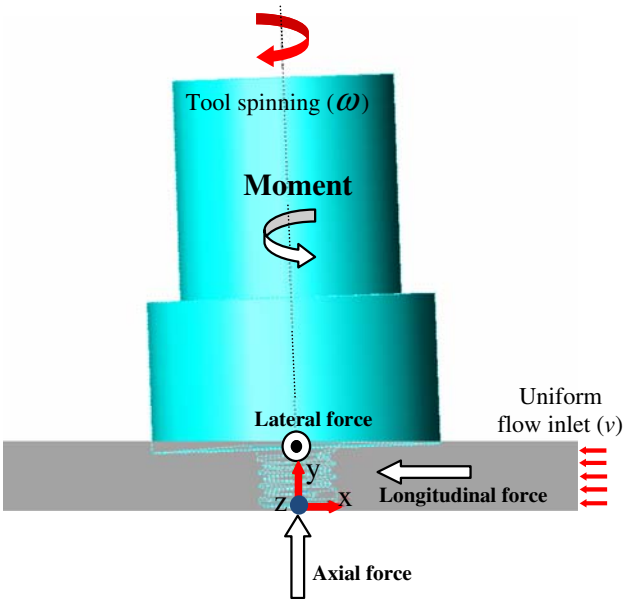

Fig. 2 Coordinate system and presumed loads applied to the FSW tool

equal to ω [= 2π*N*, *N*(rpm)]. Here, the computational zone is assumed to be a cylinder with the FSW tool located at the center, facilitating the model preparation step and saving computational time. The orthogonal Cartesian coordinate system with an origin in the center of the cylinder located at the bottom of the tool pin (see Fig. 2) is chosen in a way that the longitudinal (drag) force applied to the FSW tool is in a negative *x*-axis direction. Likewise, axial (lift) force applied to the tool is along the *y*-axis, the lateral (side) force is along the *z*-axis, and moment (torque) is about the *y*-axis.

3. Experiments—Methods and Apparatus

The aluminum alloy chosen for the experimental studies was cold-rolled, 6.3-mm thick plates of commercially available AA6061-T6 (wt. pct: 1.0 Mg, 0.6 Si, 0.28 Cu, 0.2 Cr, and bal. Al). Table 1 lists the temperature-dependant material properties of AA6061-T6 that are incorporated in the material characteristic laws and constitutive equations. The welds were performed on a retrofitted 3-axis CNC milling machine equipped with a tool-steel backing plate. In this setup, instead of tilting the FSW tool, the plates are tilted using a supporting wedge underneath the plates. The FSW tool with a smooth, concaved shoulder and one-way, right-hand threaded pin was used to accomplish the experiments. The dimensions of the tool were chosen properly based upon the thickness and material properties of the specimen to be weld. Figure 3 illustrates the FSW tool and its CAD model used for preparing the computational zone of the CFD model.

The material flow modeling of the FSW process can be conducted for steady or unsteady state conditions. Initial studies affirm that loosing intimate contact of the shoulder and specimen leads to the origination of external tunnel-like holes. Besides in a very low plunging force applied from the shoulder to the specimen, the stirring zone in the plasticized material region can hardly be developed. These phenomena initiate a high instability in the material flow regime that can be visualized when monitoring the loads applied to the tool. In this regard, the initial experiments were established to verify the validity of quasi-steady state condition assumption for the viable range of welding parameters.

Table 1 Temperature-dependent material properties used in thermo-fluidic CFD model (Ref 29)

	Temperature, K	Density, kg/m^3	Thermal conductivity, W/m °C	Heat capacity, J/Kg °C	Yield strength, MPa
AA6061	273	2700	162	917	277.7
	366.3	2685	177	978	264.6
	477.4	2657	192	1028	218.6
	588.6	2630	207	1078	66.2
	700.7	2602	223	1133	17.9
	844.1	2574	253	1230	0

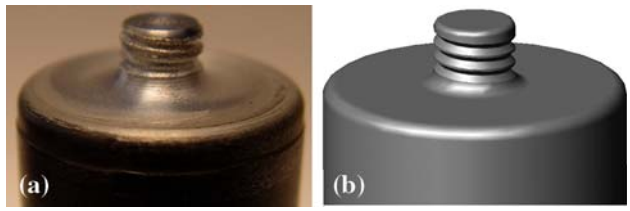

Fig. 3 FSW tool employed for accomplishing the numerical analysis and experiments; (a) the actual FSW tool and (b) CAD model

For the validated range of welding parameters resulting in the quasi-steady-state condition, the subsequent experiments were performed to verify the results of the coupled thermo-fluidic numerical simulation of the process. Therefore, experiments were setup to record the temperature history underneath the specimen at the retreating and advancing sides of the weld using K-type thermocouples. Steel-reinforced epoxy putty, FastSteel®, as an adhesive was used to bind the thermocouples to the specimen at the interface with the backing plate. The maximum temperature at five different locations, in retreating and advancing sides of the weld, were obtained and compared with the numerical results. To verify the results of the material flow model, the transient plunging (axial) force applied to the FSW tool during welding was measured for different angular and traverse velocities. The trend of variation in the plunging force was compared with the variation in the axial force for different angular and traverse velocities in the numerical analysis. Table 2 lists the welding parameters used for the experiments and lateral numerical analysis. To measure the plunging force during welding, a load cell that was incorporated into the tool holder emitted the radio signal to the antenna attached to the stationary DAQ system. The received signal was further processes, scaled, and visualized in the NI LabVIEW (Austin, TX) application software.

4. Physical Modeling and Material Properties

4.1 Assumptions and Solver Controls

Commonly in the FSW process, the specimens are prepared from cold-rolled sheets of metals that have a unidirectional

microstructure. In this study, for the sake of simplicity in the numerical modeling, the effect of the morphological and crystallographic texture of the polycrystalline material is not considered. The material is assumed to be isotropic, and no spatial direction is preferred. Besides, due to the very high viscous effect of the material, the gravitational forces are neglected. Accordingly in this study, for the presumed local model, the steady-state solution of the Navier-Stokes equations is provided for a 3-D, single phase, incompressible, viscous flow assumed for the viscoplastic material region. The CFD solver controls are set to segregated, implicit, laminar, and steady as well as the SIMPLE velocity-pressure coupling algorithm. Furthermore, the heat transfer is assumed to obey the Fourier's law of heat conduction.

4.2 The Input Model and Discretizing the Computational Region

In the FSW process, the instantaneous material flow region is small compared to the whole length of the specimen to be welded. Therefore, for the sake of simplifying the meshing step and saving the simulation time, the computational zone is assumed to be a cylinder with a diameter twice the diameter of the tool shoulder and with a height equal to the thickness of the material. Based upon this assumption, the 3-D, CAD model is prepared, translated, and exported as STEP file to the GAMBIT, a CFD preprocessor bundled with the FLUENT, for the intelligent mesh generation and boundary assignment. For the volume meshing, the T-Grid scheme with 4-node tetrahedral elements is used. Figure 4 illustrates the 2-D view of the CAD model with the boundaries and the face mesh. The features of tool pin and shoulder illustrated in Fig. 4 are basically the imprint of the bulk tool peripheral on the specimen under weld. These regions are assigned as wall zones with angular velocity boundary condition (BC). In this figure, the FSW tool consists of a cylindrical pin (Ø5.9 × 5.6 mm) and shoulder (Ø26 mm) with penetration depth of 0.3 mm. Regions U, B, and $S_{1,2}$ represent the top, bottom, and side area of the model, respectively. The present model in Fig. 4(a) and (b) shows the top surface of a cylinder (Ø52 × 6.3 mm, where 6.3 mm is the thickness of the specimen) assumed as the region for the numerical calculations of the heat transfer and fluid flow equations. Figure 4(b) illustrates the velocity inlet BC along the negative x-axis that is equal to the traverse velocity (v) of the FSW tool. Figure 4(c) shows a very fine mesh at the proximity of the FSW tool. Due to the very high strain-rate and temperature gradient in this region, the finer mesh increases the accuracy of the computational results. Nevertheless, the quality of mesh is an important factor to reach this goal. Figure 4(d) illustrates the variation of the major mesh quality index (cell equiangle skewness) with respect to the number of grids. The quality index for majority of cells is lower than 0.5 that shows a higher degree of accuracy (FLUENT 6.1 documentation). For a concise review of the mesh quality, the equiangle skewness should be checked near the boundary layer as well. It is noteworthy to mention that a dynamic mesh

Table 2 List of the welding parameters used for the experimental validations and numerical analysis

Welding condition	1	2	3	4	5	6	7	8	9	10	11	12	13	14	15	16
v, mm/min	30	90	150	210	30	90	150	210	30	90	150	210	30	90	150	210
ω, rad/s	31.4				62.8				94.2				125.6			
Penetration, mm	0.25															

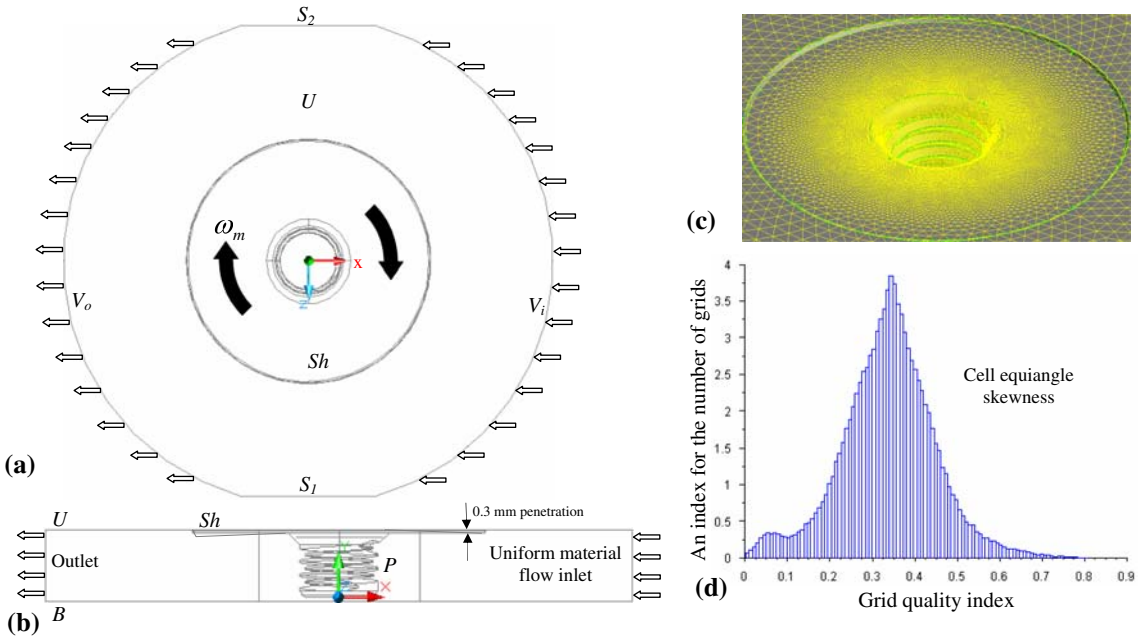

Fig. 4 CFD model preparation, (a and b) solution domain and the boundaries, (c) volume mesh near the FSW tool, and (d) the mesh quality index

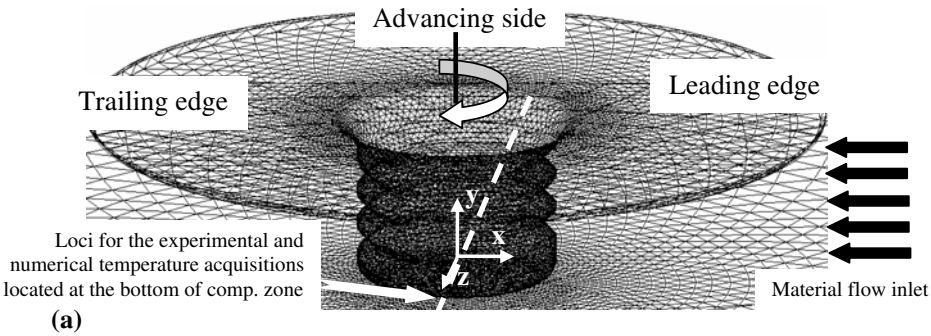

v=90 mm/min
ω=62.8 rad/sec

(b)

Fig. 5 (a) A 3-D view of the CFD model presenting the face meshes and different weld regions around the FSW tool; (b) a typical experimental outcome representing the weld bead and the pull-out location

(remesh) model is used in the FLUENT in order to compensate the rotation of an asymmetric geometry (threaded tool pin) about its axis.

Figure 5(a) illustrates a closer view of the face meshes and different regions around the FSW tool pin and shoulder. In this 3-D view, similar to Fig. 2 and 4, the material flow inlet direction is depicted along the x-axis negative direction. The trailing and leading edges as well as the advancing side of the weld are shown in Fig. 5. Figure 5(b) illustrates a typical weld bead with pull-out feature obtained employing the setup elaborated earlier.

4.3 Constitutive Laws

The flow stress ($\bar{\sigma}$) for the viscoplastic material is commonly defined as a function of equivalent plastic strain-rate tensor ($\dot{\varepsilon}_{eq}$) and the temperature (T) (Ref 26):

$$\bar{\sigma} = f(\dot{\varepsilon}_{eq}, T), \text{ when } \dot{\varepsilon}_{eq} < 1000\,(\mathrm{s}^{-1}) \qquad \text{(Eq 1)}$$

in which $\dot{\varepsilon}_{eq}$ can be calculated with the following relation:

$$\dot{\varepsilon}_{eq}^2 = \frac{2}{3}\dot{\varepsilon}_{ij}\dot{\varepsilon}_{ij} \qquad \text{(Eq 2)}$$

An expanded form of this equation is presented in (Ref 16) that is a function of the deviatoric 3-D velocity filed. In order to incorporate the solid material flow principles into a CFD solver, the viscosity of the flow needs to be defined based upon the independent variables of the flow continuum. Eq 3 presents the medium's dynamic viscosity (μ), a constitutive law for the viscoplastic materials, as a function of the equivalent strain-rate and flow stress (Ref 26):

$$\mu = \frac{\bar{\sigma}(\dot{\varepsilon}_{eq}, T)}{3\dot{\varepsilon}_{eq}} \qquad \text{(Eq 3)}$$

The flow stress $\bar{\sigma}$ is introduced by Sheppard and Wright (Ref 30) for the large and high strain-rate bulk deformation processes of metals as following:

$$\bar{\sigma} = \frac{1}{\alpha}\sinh^{-1}\left(\left(\frac{Z}{A}\right)^{1/n}\right) \qquad \text{(Eq 4)}$$

where Z is the Zenner-Holloman field variable that incorporates the effect of the continuum temperature into the flow stress equation expressed as:

$$Z = \dot{\varepsilon}_{eq}\exp\left(\frac{Q}{RT}\right) \qquad \text{(Eq 5)}$$

where R(= 8.3 J mol^{-1} K^{-1}) is the gas constant and Q (= 145 kJ mol^{-1} (Ref 31)) is the activation energy. The coefficients α, A, n, and Q are obtained from (Ref 31) for the hot extrusion of AA6061. Accordingly based on Eq 3, a user defined function (UDF) is initially incorporated into the FLUENT in order to simulate and bundle the spatially variable dynamic viscosity into the numerical calculations of the Navier-Stokes equations.

In the present model, due to the existence of the very low strain-rate outside of the TMAZ and the high strain-rate around the tool pin, the Newtonian and Non-Newtonian laws of the viscosity fields should be properly assigned to the model. An alternative method for implementing the nonlinear viscosity behavior of the material in the computational region is the Carreau viscosity model (for a generalized Newtonian fluid) (Ref 32) (FLUENT 6.1 library). This model can properly fit for both the Newtonian and non-Newtonian fluids. This model also fits very well to the viscosity of the viscoplastic material introduced in Eq 3. The Carreau viscosity model is given by:

$$\mu = \mu_\infty + (\mu_0 - \mu_\infty)\left[1 + \left(\dot{\gamma}\lambda\exp\left(\frac{T_0}{T}\right)\right)^2\right]^{\frac{(m-1)}{2}} \qquad \text{(Eq 6)}$$

where λ is the time constant, m is the power law index for the non-Newtonian fluid, $\dot{\gamma}$ is the shear strain-rate, T_0 is reference temperature, and μ_0 and μ_∞ are zero and infinite shear viscosities. Fitting this equation with the analytical results for

viscosity resolves the constants presented in the Carreau model. In this study, the constants are found to be $\mu_0 = 1e8$ m^2/s, $\mu_\infty = 0$ m^2/s, $\lambda = 10$, $T_0 = 300$ K, and $m = 0.2$. The values for viscosity based on this equation are in good agreement with the ones published in the literature (Ref 16). In comparing the numerical results with experiment in this study, the m value is tuned back and forth in order to match the results. In the numerical modeling using FLUENT, normally, it is less costly to use a viscosity model from the library of FLUENT than the one introduced as a UDF function (Eq 3). Hence, in this study, Eq 6 is used for simulating the viscosity field of the solution domain.

4.4 Conservation Equations

As described earlier, the material in the FSW process is assumed to behave as an incompressible, single-phase fluid. For this type of material, the continuity equation can be written as:

$$\frac{\partial u_i}{\partial x_i} = 0 \qquad \text{(Eq 7)}$$

where $i = 1$, 2, and 3, which represents the x, y, and z-axis, respectively. Also in this equation, u is the velocity of plastic flow. The conservation of the momentum equation in index form for the same material can be given by (Ref 33):

$$\rho \frac{\partial u_i u_j}{\partial x_i} = -\frac{\partial P}{\partial x_i} + \frac{\partial}{\partial x_i}\left(\mu \frac{\partial u_j}{\partial x_i} + \mu \frac{\partial u_i}{\partial x_j}\right) - \rho v \frac{\partial u_j}{\partial x_j} \qquad \text{(Eq 8)}$$

where ρ is the density, P is the pressure, and μ is the non-Newtonian viscosity, and the v is the free-stream velocity, or the traverse velocity.

The thermal energy conservation equation for the steady flow can be written as:

$$\frac{\partial(\rho C_p T)}{\partial t} + \nabla.(\rho C_p v T) = \nabla.(k \nabla T) + (q' + q'') \qquad \text{(Eq 9)}$$

where C_p is the specific heat capacity, k is the thermal conductivity, q' is the rate of heat input per unit volume generated by the mechanical work between the tool and specimens, and q'' is the viscous dissipation heat term.

4.5 Initial and Boundary Conditions

Recalling the zones defined in Fig. 4, the initial temperature of the medium is assumed to be 300 K. A constant linear velocity inlet BC equal to the traversing velocity (v) of the FSW tool is assumed for the zone V_i, and a flow outlet BC assigned for the zone V_o. The convection BC is assumed at the top surface (zone U) and for the sides of the computational region (zone $S_{1,2}$) with a convection heat transfer coefficient of 30 (W/m^2 K) (Ref 8). At the bottom surface (zone B), due to the intimate contact of the specimens to the backing plate, an effective contact heat transfer coefficient is assumed to match with the experimentally measured temperature. In an attempt for matching the temperature results, it was found that the contact heat transfer coefficient is sensitive to the temperature range at the zone B.

In order to define the heat input and BC of the tool pin and shoulder, the interfacial contact condition between the FSW tool and the surrounding material needs to be defined. Here the partial sliding/sticking state of the contact is assumed as defined by Schmidt et al. (Ref 34). They proposed a state variable δ that relates the rotational velocity of the surrounding material and the FSW tool. This dimensionless variable is defined as: $\delta = \omega_m/\omega = 1 - \dot{\gamma}/\omega$, $0 < \delta < 1$, where ω_m is the angular velocity of the material in contact, and $\dot{\gamma}$ is the slipping rate. Schmidt et al. concluded that the contact situation is closer to the sticking condition by comparing the analytical and experimental plunging force and the heat generations. Likewise in this study, the partial slipping/sticking condition is assumed with sticking extent or state variable δ equal to 0.65 (Ref 35). Therefore, a constant angular velocity BC for the pin (zone P) and shoulder (zone Sh) (see Fig. 4a and b) is assumed to be equal to ω_m that is the angular velocity of the material in contact with the FSW tool. Zone P includes the threaded side area, tip, and the filleted root area of the tool pin. Zone Sh includes the shoulder and the filleted area at the peripheral. Consequently, the heat generation in the FSW process due to the friction and plastic work in the contact area of the tool with the surrounding material may be assumed as a heat flux (Ref 34) at the pin, shoulder, and specimen interface and can be expressed as:

$$q'(r) = q_1 + q_2(r), \quad r_{\text{pin}} < r \le r_{\text{shoulder}} \qquad \text{(Eq 10)}$$

where

$$q_1 = q_{\text{pin}} = \delta r_p \omega_m \tau_{\text{yield}} + (1-\delta)\mu_k P \qquad \text{(Eq 11)}$$

and

$$q_2(r) = q_{\text{shoulder}} = \delta r \omega_m \tau_{\text{yield}} + (1-\delta)\mu_k P \qquad \text{(Eq 12)}$$

where μ_k is kinetic friction coefficient assumed to be 0.4 (Ref 35), τ_{yield} is the extent of the shear stress for yielding equal to $\sigma_y/\sqrt{3}$ which obeys the von Mises yielding criterion. Here in the heat flux Eq 11 and 12, the effect of longitudinal velocity of material on the linear velocity ($r_p\omega_m$ and $r\omega_m$) is neglected.

Another significant thermal energy source contributing in temperature increase and material deformation is the inter-layer shearing of material. This source incorporates the thermal energy created by the viscous shearing of the material flow and appears in the energy equation as viscous dissipation term. This heat input (q'') is important to include if the Brinkman number ($Br = \mu v^2/k\delta T$) exceeds the unity that is estimated to be valid for the TMAZ and nugget zones of the weld. Therefore, the cumulative thermal energy input is the summation of the viscous heating and the heat flux from the FSW tool pin and shoulder.

5. Results and Discussion

For the butt FSW of AA6061-T6 under different welding parameters, the 3-D local material flow and heat transfer analysis were performed. The viscous energy as well as the frictional heating generated at the contact surfaces of the tool and the surrounding materials was assumed as the only heat inputs for the numerical modeling. To increase the accuracy of the model and obtain a reliable estimation of the loads extent, an FSW tool with a one-way right-handed thread on a cylindrical pin and concaved shoulder with a tool rake-angle of 2.5 degrees were assumed in the CFD model.

5.1 Model Verifications

5.1.1 Temperature. Temperature is measured at the bottom surface of the specimen in five different locations along the z-axis (see Fig. 5a). Temperature profiles are obtained for each

of the locations, and the maximum values are registered when the tool passed by the thermocouples. The utmost measured temperature values are plotted in Fig. 6 as experimental data. Numerically calculated maximum temperature values are also determined for the same locations based on the average cell temperature and are plotted as numerical values in Fig. 6. The horizontal axis in this figure represents the distance from the center point of the tool. From this figure, it can be observed that the advancing side has higher values of temperature in both the experimental and numerical studies, as was previously confirmed by Schmidt and Hattel (Ref 34). These values are because of the existence of the higher relative velocity that causes more rigorous viscoplastic material shearing and results in higher heat generation by the plastic deformation and viscous heating. As an alternative representation, Fig. 7 illustrates the contour graph of the thermal gradient of the material surrounding the FSW tool. In this figure, the numerically calculated maximum temperature region is observed at the contact surface of the computational zone and the shoulder at a particular distance from the center of the FSW tool. The results shown in Fig. 6 and 7 are consistent with most of the numerical and experimental values published in literature (Ref 8, 16, 34).

5.1.2 Axial Force. A typical plot of axial force versus time is shown in Fig. 8. Various features on the plot represent different process status. The initial local maxima of the axial force, for instance, may represent the time where the tool pin penetrates the specimen that is work-hardened under rigorous compression (tool plunging) and shear stress (tool rotation). Considering the tool traversing zone in Fig. 8, in this study, the experimentally recorded axial force in the *process stable condition* is compared with the numerical results.

Figure 9 illustrates the comparison between the experimental and (mean value of) numerical axial forces applied to the tool under the FSW tool angular and traverse velocities that vary from 31.2 to 125.6 rad/s and from 30 to 210 mm/min, respectively. Here, the numerical axial force is calculated based on the reference values listed in Table 3.

Looking at Fig. 9, the higher angular and lower traverse velocities initiate a higher axial force in both experimental and numerical results. In this figure, a very good agreement is found between the numerical and experimental results where the tool angular velocity is between 90 and 110 rad/s. However, at the lowest (31.2 rad/s) and highest (125.6 rad/s) angular velocities, there are mismatches of about 20% and 5%, respectively, between the experimental and numerical results. The slight mismatches under some welding parameters might arise due to a fixed state variable assumption ($\delta = 0.65$) in the numerical model. A welding condition-dependant slipping rate may increase the accuracy of the numerical model.

5.2 Viscosity Field

Figure 10 shows a comparison of the cross-section of the weld and iso-contours of the viscosity during FSW with the identical process parameters. Locating the TMAZ

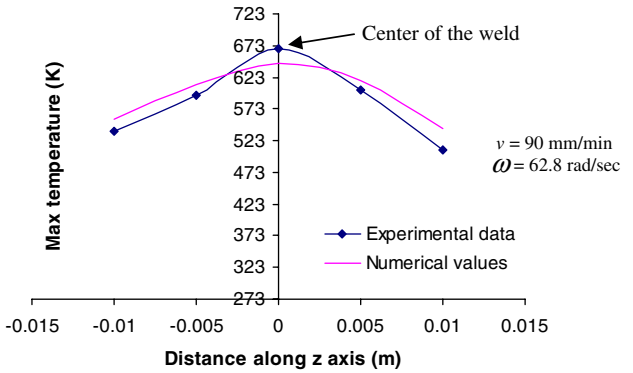

Fig. 6 A typical comparison of experimental and numerical results presenting the maximum temperature underneath the specimen

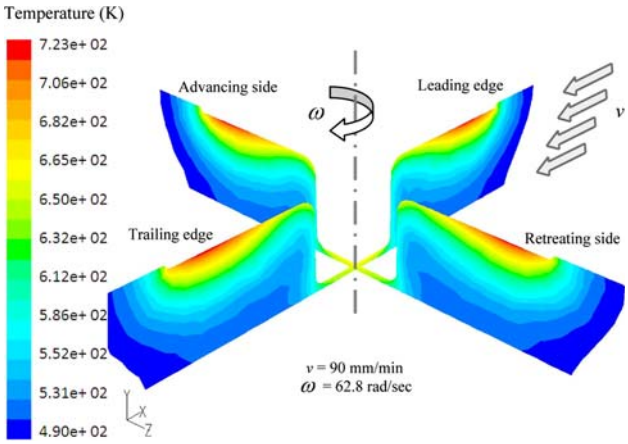

Fig. 7 Numerical results showing the contour graph of the thermal gradient in the computational zone surrounding the FSW tool

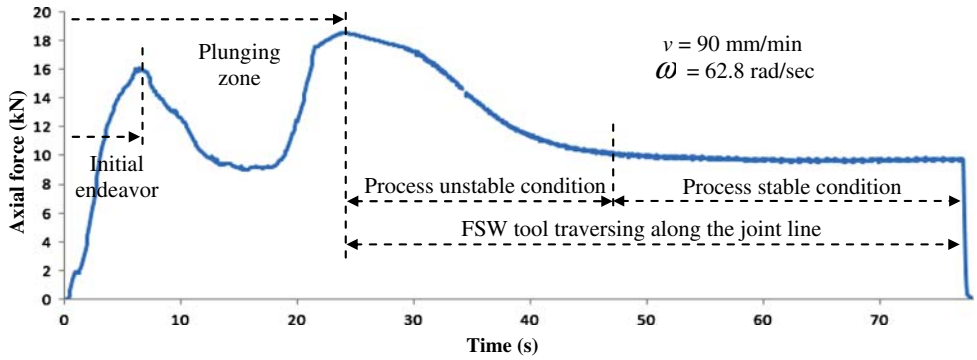

Fig. 8 Transient axial force applied to the FSW tool

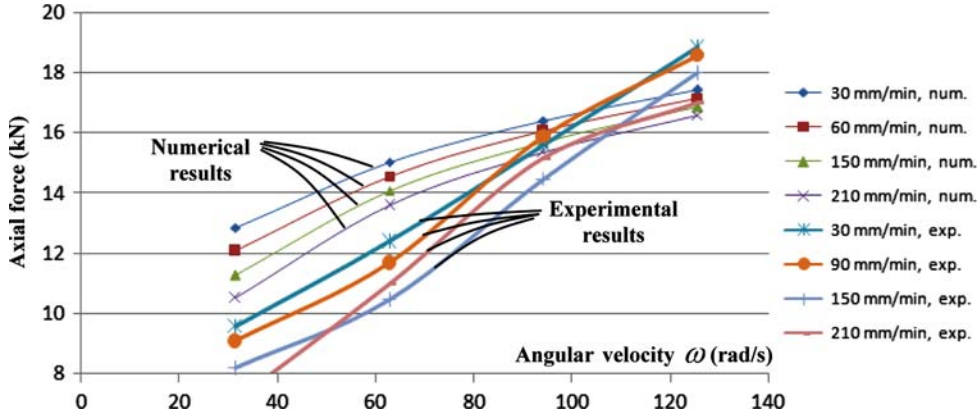

Fig. 9 Comparison of the steady axial force in the numerical model and experiments

Table 3 Characteristic values used in the numerical computation of the axial force

Temperature, K	Area, m^2	Density, kg/m^3	Length, m	Velocity, m/s	Pressure, Pa
300	1	2700	1	1	0

region – based on the microscopic studies – approximately on the cross-section of the weld, a similar morphology on the viscosity contour plot can be observed with the iso-region limited to 4.3×10^6 kg/(m s). This concluded value is in good agreement with the similar analysis reported in literature (Ref 16).

5.3 Forces and Moment

5.3.1 Loads on the Tool Pin. Figure 11 illustrates the variation of the various loads applied to the tool pin with changing the welding parameters. In this figure, the effects of the inertia and viscous forces are shown distinctively in order to distinguish the impact of material flow pressure and the shear stresses on the resultant loads.

Figure 11(a) illustrates the inertia and viscous effects of the material flow on the longitudinal force applied to the tool pin. Increasing the angular velocity decreases the magnitude of the longitudinal inertia and viscous forces due to the higher heat input that decreases the viscosity in the TMAZ region. However, increasing traverse velocity augments the magnitude of the longitudinal forces thus may increase the tool wear and the chance of tool failure. As apparent, the viscous and inertia forces have almost the same order of magnitude in changing the longitudinal force applied to the tool pin. Nevertheless, inertial effects have more been pronounced in the higher traverse and lower angular velocities due to the higher pressure deviation on the pin wall than the shear stresses caused by the lower angular velocity.

Figure 11(b) shows the extent of the axial force applied to the tool pin with changing the welding parameters. Higher angular and traverse velocities initiate a higher axial force. This plot depicts that the viscous force slightly changes the extent of the axial force. Again, the inertia force has an additive effect on the axial force because of the projection surface of the pin with respect to the axial force vector (see Fig. 1). As Fig. 11(c) shows, the lateral force caused by the Magnus effect in the computational zone, is augmented by the viscous forces that remain almost constant with changing the welding parameters. However the inertia effect, regardless of its lower extent, augments the lateral force in the higher traverse velocity range but in a negative z-axis direction. This phenomenon will be readily concluded if the dynamic pressure distribution in retreating and advancing sides of the weld is studied (Ref 36, 37). Plotting of the moment in Fig. 11(d) shows that the inertia has an insignificant effect on the moment applied to the tool pin around the FSW tool axis. However, the viscous moment initiated by the shear stress on the tool pin has a significant impact on the moment, and the viscous moment is augmented in the lower angular and higher traverse velocities.

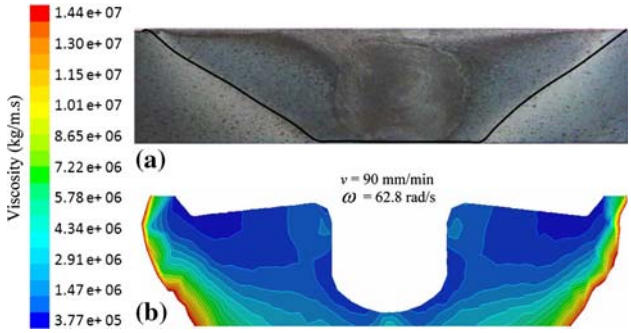

Fig. 10 A typical comparison between the experimental and numerical result, (a) weld cross-section showing the TMAZ region (b) contour graph of the dynamic viscosity

5.3.2 Loads on the Tool Shoulder. Similarly, Fig. 12 illustrates the 3-D plot of the variation of the loads applied to the tool shoulder while changing the welding parameters. The plot of Fig. 12(a) shows that the viscous and inertia effects have almost the same order of magnitude when altering the longitudinal force applied to the tool shoulder. A maximum of longitudinal force is found at the highest traverse and lowest angular velocity. This result is because increasing the angular velocity increases the temperature, and therefore decreases the dynamic viscosity that reduces the amount of the longitudinal force. However, increasing the traverse velocity augments the dynamic pressure distribution deviation along the welding pass, which increases the longitudinal force applied to the tool shoulder.

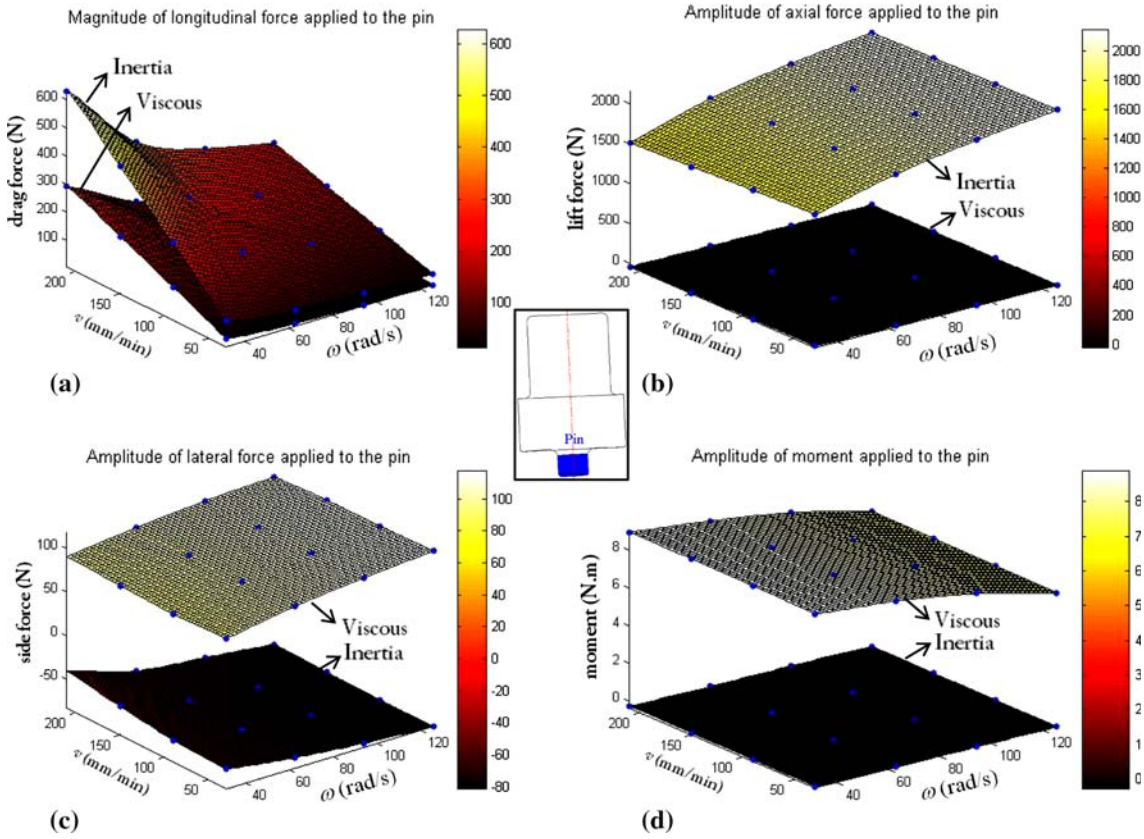

Fig. 11 Numerical results of the loads applied to the tool pin varied with changing the welding parameters

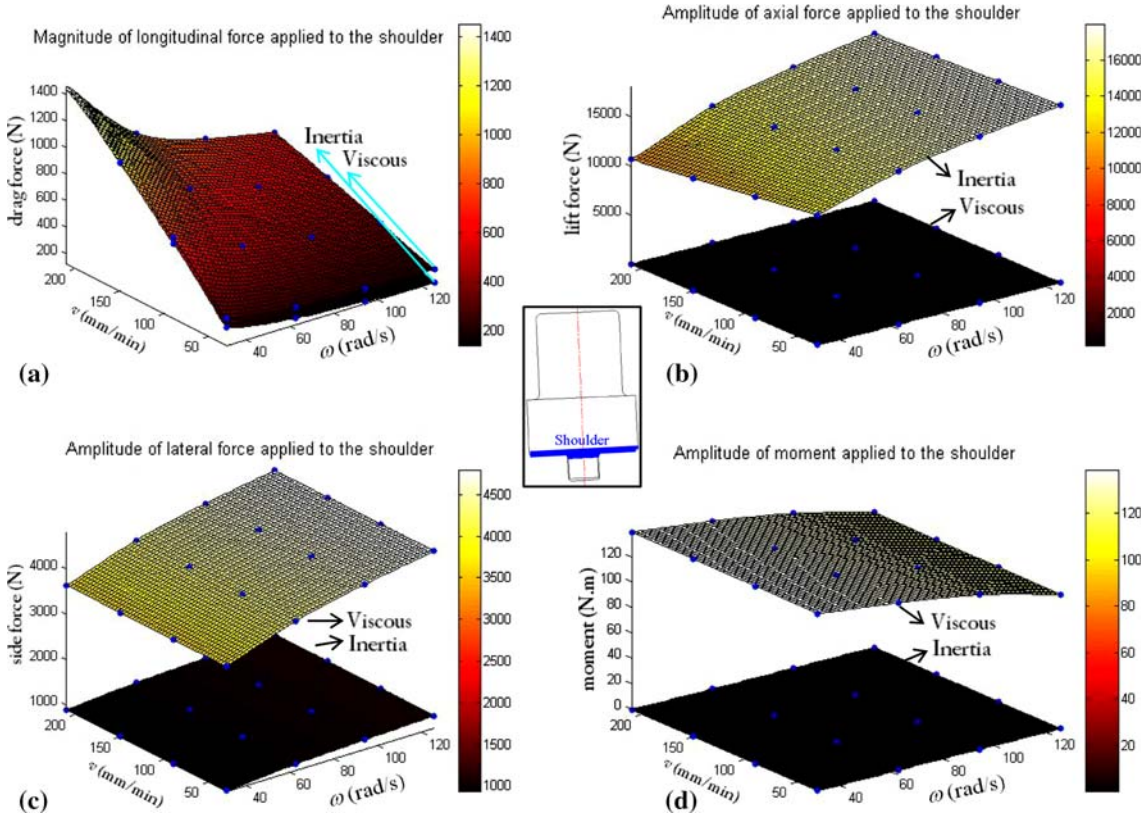

Fig. 12 Numerical results of the loads applied to the tool shoulder with changing the welding parameters

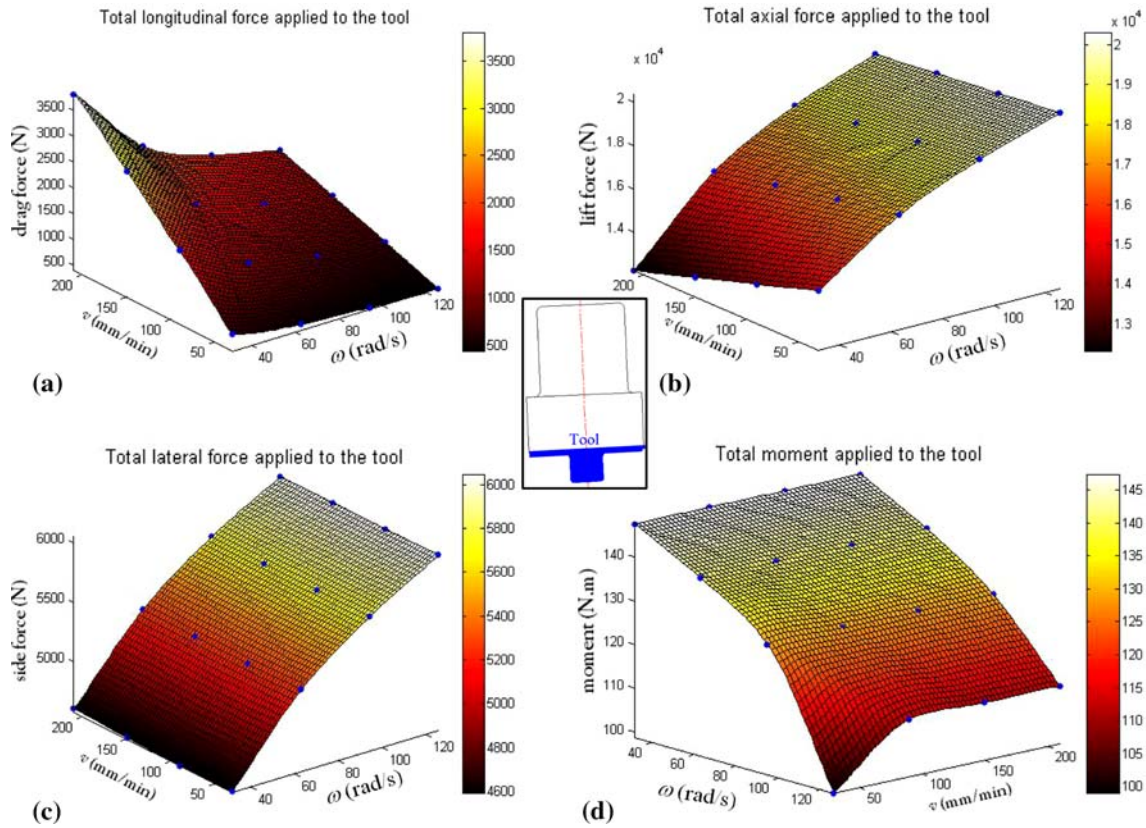

Fig. 13 Numerical results of the total loads applied to the FSW tool with changing the welding parameters

The variation of inertia and viscous axial force applied to the tool shoulder is shown in Fig. 12(b). Similar to Fig. 11(b), this plot shows that the viscous force has insignificant vector element magnitude along the presumed axial force vector (y-axis, see Fig. 5a). The inertia force dominantly contributes in relation to the amount of the axial force applied to the tool shoulder. The axial force reaches the extreme amount in the highest angular and lowest traverse velocities. This phenomenon may be readily verified if the dynamic pressure distribution along the weld cross-section was studied (Ref 36, 37). Plot of Fig. 12(c) illustrates the lateral force variation with welding parameters that resembles the domination of the viscous over inertia forces. In this figure, the lateral force is maximum in the highest angular velocity; whereas, the traverse velocity impact on the lateral force appears to be insignificant.

Figure 12(d) depicts the 3-D plot of the resistive moment variation applied to the tool shoulder while changing the welding parameters. Accordingly, the viscous effects dominate in initiating the resistive moment, and the extreme amount of the moment is obtained at the highest angular velocity. However, the traverse velocity appears to have much less impact on the extent of the moment. Similar to the moment applied to the tool pin, Fig. 12(d) shows that the inertia effects have insignificant impact on the moment applied to the tool shoulder.

5.3.3 Cumulative Loads Carried by the FSW Tool. In order to test the mechanical strength, wear resistivity, and the stress field of the FSW tool, it is required to simultaneously estimate the cumulative amount of the viscous and inertia loads applied to the tool pin and shoulder, altogether. In addition, the computed loads may be applied in designing the clamping system of the welding setup. Accordingly, Fig. 13 illustrates the variation of forces and moment carried by the FSW tool while changing the welding parameters. The plot of the longitudinal force in Fig. 13(a) shows that increasing the angular velocity decreases the magnitude of the longitudinal force; however, increasing traverse velocity increases the magnitude of the longitudinal force. The maximum amount of longitudinal force is obtained when the tool angular velocity is minimum (31.4 rad/s), and the traverse velocity of the tool is maximum (210 mm/min). The minimum amount of longitudinal force is obtained when the angular velocity reaches to the maximum value (125.6 rad/s) and the traverse velocity is minimum. This plot implies that in order to obtain high speed welding with lower resistive force on the FSW tool, it is required to increase both the angular and traverse velocities of the process. The plot of Fig. 13(b) shows the variation of total axial force by changing the welding parameters. The minimum axial force is found to be in the minimum amount of the angular and maximum amount of the traverse velocity. Accordingly, increasing the angular and decreasing the traverse velocity augments the amount of the total axial force applied to the FSW tool. Figure 13(c) illustrates the amount of the total lateral force which is increased significantly by increasing the angular velocity. However, the traverse velocity of the FSW tool has a trivial impact on the amount of the lateral force.

Studying the amount of resistive moment applied to the FSW tool is crucial in estimating the required power to accomplish a typical FSW process. Figure 13(d) depicts the variation of the total moment applied about the FSW tool axis.

The minimum amount of the moment is found when the angular velocity is maximum and the traverse velocity is minimum, because of the accumulation of the thermal energy that results in the lower viscosity field. In this figure, increasing the angular velocity decreases the moment applied to the FSW tool with a higher rate of descending at a lower traverse velocity range. However, the effect of traverse velocity variation on the moment appears to be insignificant mainly at the lower angular velocity range.

5.4 Required Power

Estimating the consumed power of a typical FSW process is essential in determining the hardware and the cost of process operation. The required power for accomplishing the FSW process on a retrofitted CNC milling machine is in direct relation with the torque and angular velocity applied to the FSW tool as described below.

$$P = \omega \left[\int_{r=0}^{r=r_p} M_{1,p}(r)dr + M_{2,p}(r_p) + \int_{R=r_p}^{R=r_s} M_s(R)dR \right] \quad \text{(Eq 13)}$$

where $M_{1,p}$ is the moment applied to the tool pin bottom surface, $M_{2,p}$ is the moment applied to the lateral surface area of the tool pin, M_s is the moment applied to the tool shoulder, and r_p and r_s are the average pin and shoulder radii, respectively. This relation shows that there is no direct relation between the traverse velocity of the FSW tool and the consumed power. However, the moments (M) are being affected slightly by the traverse velocity because it alters the temperature distribution and the viscosity field of the computational domain. It is noteworthy to mention that the $M_{1,p}$, $M_{2,p}$, and M_s in Eq 13 are the combined result of viscous and inertia moments applied to the FSW tool. The attained power consumed for the FSW process with presumed conditions in this study is shown in Fig. 14. This plot declares that the consumed power is maximum when the angular and traverse velocities are in the ultimate range. The effect of the traverse velocity on the consumed power is more pronounced at an extreme angular velocity; however, in the lower angular velocity range, the effect of traverse velocity on the consumed energy appears to be insignificant.

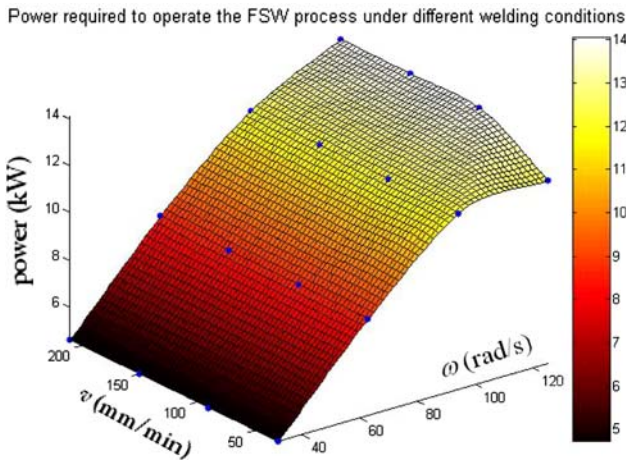

Fig. 14 Numerically computed consumed power in different welding conditions for presumed FSW setup

6. Conclusions

A 3-D numerical analysis of heat transfer and material flow is presented for the butt FSW of AA6061-T6 to investigate the weld physical properties and the loads applied to the FSW tool. The temperature-dependant material properties as well as the generalized Newtonian viscosity model (Carreau model) are considered for the presumed viscoplastic material model. The CFD model is developed including the concave tool shoulder and cylindrical, right-hand, threaded tool pin. Based upon the sliding/sticking condition assumption for the FSW tool (state variable $\delta = 0.65$) and after the experimental investigations and verifications, the main observations are as follows:

1) Brinkman number (Br) exceeds the unity for the nugget and TMAZ zones in the FSW process. Therefore, the viscous heating term may be considered in order to obtain a true simulation of the process.
2) Comparing with the proposed simulations in the literature, the current numerical results show that including the sliding/sticking behavior promotes the accuracy of the numerical results; however, the state variable needs to be adjusted for different welding parameters in order to obtain the accurate computational results in various weld conditions.
3) Good agreements between the numerical and experimental results may imply that the Carreau viscosity model can properly simulate the viscosity field in the FSW process thus saving the computational time of using UDF functions.
4) The maximum temperature in the computational zone is found to be less than the minimum melting (eutectic) temperature [823 K (Ref 38)] of AA6061 for different welding parameters. Additionally, a comparison of the TMAZ region with the iso-lines on the dynamic viscosity contour plot represents a similar zone, with the viscosity limited to 4.3×10^6 kg/(m s).
5) The longitudinal force applied to the FSW tool is mainly affected by the traverse velocity. However, the angular velocity has a major impact on the extent of the axial force, lateral force, and moment applied to the tool.
6) Inertia and viscous forces have almost the same order of magnitude in initiating the longitudinal force applied to the tool. Nevertheless, viscous effects are insignificant in initiating the axial force, and the inertial effects are insignificant in initiating the lateral and moment applied to the tool.
7) The total required power is affected significantly by changing the angular velocity of the tool. Furthermore, the power is varied by the traverse velocity solely at the higher angular velocities.

This model may be extended to visualize the effect of advanced features of the FSW tool on the extent of the loads. Additionally, using the parametric model design, an optimized feature of the FSW tool with minimum longitudinal load may be obtained in order to employ the highest welding speed in the mass production. Furthermore, in the realm of the numerical simulation, sensitivity analyses of the primary parameters may be performed in order to present the contribution of the parameters on the final results.

Acknowledgments

This work is supported by the Research Center for Advanced Manufacturing (RCAM) at Southern Methodist University and partially supported by Millersville University of Pennsylvania. Authors would like to thank Dr. B. Antohe at MicroFab Inc. for thoughtful insights and for assistance in preparing the 3-D grid of the solution domain.

References

1. W.M. Thomas, E.D. Nicholas, J.C. Needham, M.G. Murch, P.T. Smith, and C.J. Dawes, International Patent No. PCT/GB92/02203, GB Patent No. 9125978.8 (1991), US Patent No. 5,460,317 (1995)
2. J.H. Ouyang and R. Kovacevic, Material Flow and Microstructure in the Friction Stir Butt Welds of the Same and Dissimilar Aluminum Alloys, *J. Mater. Eng. Perfom.*, 2002, **11**(1), p 51–63
3. W.J. Arbegast, Friction Stir Welding After a Decade of Development, *Weld. J.*, 2006, **85**(3), p 28–35
4. H.R. Shercliff, J. Michael, M.J. Russell, A. Taylor, and T.L. Dickerson, Microstructural Modeling in Friction Stir Welding of 2000 Series Aluminum Alloys, *Mec. Indust.*, 2005, **6**, p 25–35
5. Y.S. Sato, S.H. Park, and H. Kokawa, Microstructural Factors Governing Hardness in Friction Stir Welds of Solid-Solution-Hardened Al Alloys, *Metall. Mater. Trans. A*, 2001, **32**, p 3033
6. T.J. Lienert, W.L. Stellwag, B.B. Grimmett, and R.W. Warke, Friction Stir Welding Studies on Mild Steel, *Weld. J.*, 2003, p 1–9
7. P.A. Colegrove and H.R. Shercliff, Development of Trivex Friction Stir Welding Tool, Part 1—Two-Dimensional Flow Modeling and Experimental Validation, *Sci. Technol. Weld. Join.*, 2004, **9**(4), p 345–351
8. Y.J. Chao, X. Qi, and W. Tang, Heat Transfer in Friction Stir Welding—Experimental and Numerical Studies, *J. Manuf. Sci. Eng.*, 2003, **125**, p 138–145
9. P. Heurtier, M.J. Jones, C. Desrayaud, J.H. Driver, F. Montheillet, and D. Allehaux, Mechanical and Thermal Modeling of Friction Stir Welding, *J. Mater. Process. Technol.*, 2006, **171**, p 348–357
10. M. Guerra, C. Schmidt, J.C. McClure, L.E. Murr, and A.C. Nunes, Flow Patterns During Friction Stir Welding, *Mater. Charact.*, 2003, **49**, p 95–101
11. B. London, M. Mahoney, W. Bingel, M. Calabrese, and D. Waldron, Experimental Methods for Determining Material Flow in Friction Stir Welds, *Presented at the 3rd International Symposium on Friction Stir Welding (Kobe, Japan)*, Sep 2001, p 4–7
12. K. Colligan, Material Flow Behavior During Friction Stir Welding of Aluminum, *Weld. J.*, 1999, **75**(7), p 229–237
13. L. Ke, X. Li, and J.E. Indacochea, Material Flow Patterns and Cavity Model in Friction-Stir Welding of Aluminum Alloys, *Metall. Mater. Trans. B*, 2004, **35**, p 153–160
14. T.U. Seidel and A.P. Reynolds, Visualization of Material Flow in AA2195 Friction Stir Welds Using a Marker Insert Technique, *Metall. Mater. Trans. A*, 2001, **37**, p 2879–2884
15. P.A. Colegrove and H.R. Shercliff, 3-Dimensional CFD Modelling of Flow Round a Threaded Friction Stir Welding Tool Profile, *J. Mater. Process. Technol.*, 2005, **169**, p 320–327
16. R. Nandan, G.G. Roy, and T. DebRoy, Numerical Simulation of Three-Dimensional Heat Transfer and Plastic Flow During Friction Stir Welding, *Metall. Mater. Trans. A*, 2006, **37**, p 1247–1259
17. S. Xu, X. Deng, A.P. Reynolds, and T.U. Seidel, Finite Element Simulation of Material Flow in Friction Stir Welding, *Sci. Technol. Welding Joining*, 2001, **6**(3), p 191–193
18. R. Crawford, G.E. Cook, A.M. Strauss, D.A. Hartman, and M.A. Stremler, Experimental Defect Analysis and Force Prediction Simulation of High Weld Pitch Friction Stir Welding, *Sci. Technol. Welding Joining*, 2006, **11**(6), p 657–665
19. C. Chen and R. Kovacevic, Thermomechanical Modelling and Force Analysis of Friction Stir Welding by the Finite Element Method, *Proc. IME C J. Mech. Eng. Sci.*, 2004, **218**(5), p 509–519
20. R. Johnson, Forces in Friction Stir Welding of Aluminum Alloys, *Presented at the 3rd International Symposium on Friction Stir Welding (Kobe, Japan)*, Sep 2001, p 6–19
21. J.W. Pew, "A Torque-Based Weld Power Model for Friction Stir Welding", M.Sc. Thesis, Brigham Young University, 2006
22. D. Jandric, M. Chen, M. Valant, and R. Kovacevic, Characterization of Weld Quality by Different Sensing Techniques in Friction Stir Welding of Lap Joints, *Presented at 4th International Symposium on Friction Stir Welding (Park City, Utah)*, May 2003, p 6
23. R.R. Itharaju, "Friction Stir Processing of Aluminum Alloys," M.Sc. Thesis, University of Kentucky, 2004
24. Y.T. Chew, M. Cheng, and S.C. Luo, A Numerical Study of Flow Past a Rotating Circular Cylinder Using a Hybrid Vortex Scheme, *J. Fluid Mech.*, 1995, **299**, p 35–71
25. S. Mittal and B. Kumar, Flow Past a Rotating Cylinder, *J. Fluid Mech.*, 2003, **476**, p 303–334
26. O.C. Zienkiewicz, P.C. Jain, and E. Onate, Flow of Solids During Forming and Extrusion: Some Aspects of Numerical Solutions, *Int. J. Solid Struct.*, 1978, **14**, p 15–38
27. W.J. Arbegast, Modeling Friction Stir Joining as a Metalworking Process, *Proceedings of Symposium on Hot Deformation of Aluminum Alloys III*, March 2-6, 2003 (San Diego, California), TMS, p 313–327
28. N. Cristescu and I. Suliciu, Viscoplasticity (Mechanics of Plastic Solids). Kluwer Academic Publishers, Dordrecht, 1982
29. P. Dong, F. Lu, J.K. Hong, and Z. Cao, Coupled Thermomechanical Analysis of Friction Stir Welding Process Using Simplified Models, *Sci. Technol. Welding Joining*, 2001, **6**(5), p 281–287
30. T. Sheppard and D.S. Wright, Determination of Flow Stress I-Constitutive Equation for Aluminum Alloys at Elevated Temperatures. II-Radial and Axial Temperature Distribution During Torsion Testing, *Met. Tech.,* 1979, **6**, 215–229
31. T. Sheppard and A. Jackson, Constitutive Equations for Use in Prediction of Flow Stress During Extrusion of Aluminum Alloys, *Mater. Sci. Tech.*, 1979, **13**(3), p 203–209
32. R.I. Tanner, *Engineering Rheology*, 2nd ed., Oxford University Press, May 2000
33. W. Zhang, G.G. Roy, J. Elmer, and T. DebRoy, Modeling of Heat Transfer and Fluid Flow During Gas Tungsten Arc Spot Welding of Low Carbon Steel, *J. Appl. Phys.*, 2003, **93**(5), p 3022–3033
34. H.N.B. Schmidt and J. Hattel, Heat Sources Models in Simulation of Heat Flow in Friction Stir Welding, *Int. J. Offshore Polar Eng.*, 2004, **14**(4), p 296–304
35. M. Song and R. Kovacevic, Heat Transfer Modelling for Both Workpiece and Tool in the Friction Stir Welding Process: A Coupled Model, *Proc. IME. B J. Eng. Manufact.*, 2004, **218**(1), p 17–33
36. H. Atharifar and R. Kovacevic, Computational Study on the Qualitative Effect of Process Parameters on the Forces and Torque Applied to the Tool in Friction Stir Welding, *Presented at ASME GSRIC Conference (Tulsa, OK)*, April 2007
37. H. Atharifar and R. Kovacevic, Numerical Study of the Tool Rake Angle Affect on the Material Flow in Friction Stir Welding Process, *Presented at ASME International Mechanical Engineering Congress and Exposition (Seattle, WA)*, Nov 2007
38. L.F. Mondolfo, *Aluminum Alloys: Structure and Properties*, Butterworth & Co., Boston, MA, 1976, p 717–857